

# A near-infrared and optical photometric study of the Sculptor dwarf spheroidal galaxy: implications for the metallicity spread

C. Babusiaux<sup>1,2</sup>, G. Gilmore<sup>1</sup>, M. Irwin<sup>1</sup>

<sup>1</sup> *Institute of Astronomy, University of Cambridge, Cambridge, CB30HA, UK*

<sup>2</sup> *Institut d’Astronomie et d’Astrophysique, Université Libre de Bruxelles, B-1050 Bruxelles*

Accepted xxx. Received xxx

## ABSTRACT

The Sculptor dwarf spheroidal galaxy has a giant branch with a significant spread in colour, symptomatic of an intrinsic age/metallicity spread. We present here a detailed study of the Sculptor giant branch and horizontal branch morphology, combining new near-infrared photometry from the Cambridge InfraRed Survey Instrument (CIRSI), with optical data from the ESO Wide Field Imager. For a Sculptor-like old and generally metal-poor system, the position of Red Giant Branch (RGB) and Asymptotic Giant Branch (AGB) stars on the colour-magnitude diagram (CMD) is mainly metallicity dependent. The advantage of using optical-near infrared colours is that the position of the RGB locus is much more sensitive to metallicity than with optical colours alone. In contrast the horizontal branch (HB) morphology is strongly dependent on both metallicity and age. Therefore a detailed study of both the RGB in optical-near infrared colours and the HB can help break the age-metallicity degeneracy. Our measured photometric width of the Sculptor giant branch corresponds to a range in metallicity of 0.75 dex. We detect the RGB and AGB bumps in both the near-infrared and the optical luminosity functions, and derive from them a mean metallicity of  $[M/H] = -1.3 \pm 0.1$ . From isochrone fitting we derive a mean metallicity of  $[Fe/H] = -1.42$  with a dispersion of 0.2 dex. These photometric estimators are for the first time consistent with individual metallicity measurements derived from spectroscopic observations. No spatial gradient is detected in the RGB morphology within a radius of 13 arcminutes, twice the core radius. On the other hand, a significant gradient is observed in the HB morphology index, confirming the ‘second parameter problem’ present in this galaxy. These observations are consistent with an early extended period of star formation continuing in time for a few Gyr.

**Key words:** galaxies: individual: Sculptor dwarf spheroidal – galaxies: stellar content – Local Group – infrared: stars

## 1 INTRODUCTION

The dwarf galaxies of the Local Group offer a unique opportunity to quantify the evolution and interactions of low-mass galaxies. Dwarf spheroidals were originally thought to be very similar in their metallicity and star formation histories to the galactic globular clusters, but their star formation history is now known to be more complex. The Sculptor dwarf spheroidal, the first dSph discovered (Shapley 1938), has a population which is predominantly old and moderately metal poor (e.g. Da Costa 1984, Mateo 1998, Monkiewicz & et al. 1999, Dolphin 2002). However, the presence of an extended horizontal branch (e.g. Da Costa 1984, Majewski et al. 1999) and the detection of associated neutral hydrogen (Carignan et al. 1998,

Bouchard et al. 2003) suggest the possibility of a more complex star formation history. A metallicity spread has been inferred in Sculptor from the large spread of its red giant branch (e.g. Da Costa 1984, Schweitzer et al. 1995, Kaluzny et al. 1995, Majewski et al. 1999) and the period distribution of RR Lyrae (Kaluzny et al. 1995, Kovács 2001). Metallicity gradients have been discovered in several dwarf spheroidals (Harbeck et al. 2001). Majewski et al. (1999) and Hurley-Keller et al. (1999) showed that the red horizontal branch (RHB) of Sculptor is more strongly concentrated towards the centre than is the bluer population. Majewski et al. (1999) suggest this and the detection of two bumps in the Sculptor red giant branch are direct evidence for a bimodality in Sculptor’s metallicity distribu-

tion. Hurley-Keller et al. (1999) find no radial gradient of the age or metallicity distribution within Sculptor, whereas using the same data, Harbeck et al. (2001) find a metallicity gradient. Spectroscopic studies of a few stars in the central regions confirmed a wide abundance range, over 1 dex (Shetrone et al. 2003), while first results from an extensive spectroscopic study of Tolstoy et al. (2004) confirm the broad abundance distribution, with range  $-2.5 < [\text{Fe}/\text{H}] < -1.5$ , and show that the central regions, where the RHB stars are found, also contains a significant subpopulation of stars as metal rich as -1 dex.

Photometric studies of the age distribution in Sculptor (Monkiewicz & et al. 1999, Dolphin 2002 and Rizzi et al. 2004) confirm that a significant metallicity gradient, with some relatively smaller age spread, are both required by the stellar colour-magnitude diagram, and are consistent with all other data. This predominately old age is puzzling, given that Sculptor is apparently unique among the dSph galaxies in having associated HI. Sculptor is further of interest in that it may belong to a common orbital plane with several other dSph (Lynden-Bell 1976).

In this paper we present the first near-infrared photometric study of Sculptor. The combination of our near-infrared data, obtained with the Cambridge InfraRed Survey Instrument (CIRSI) on the Las Campanas 2.5m duPont telescope, and optical data from the ESO 2.2m Wide Field Imager archive, has allowed us to undertake a broader waveband study of the metallicity spread in Sculptor. Observations and data reduction procedures are presented in Section 2. In Section 3 colour-magnitude diagrams of Sculptor are compared with theoretical isochrones and globular cluster data. In section 4 we present the detection of the RGB and AGB bumps. The metallicity distribution function is derived in section 5. Section 6 is devoted to the study of the variation of RGB and HB morphologies with radius. We conclude with a discussion of the main results.

## 2 THE DATA

Photometric studies provide a valuable tool to determine internal metallicity spreads in dSph galaxies. Although individual spectroscopic measurements are more precise, as yet the numbers of stars with direct spectra is small. Most such photometric studies use optical photometry. The combination of optical and near-infrared data provides substantially enhanced information, reducing the effect of photometric errors, allowing colour-colour selection of sources, and providing in particular the V-K colour, which is a good indicator of the stellar effective temperature.

We have obtained wide-area near-infrared J and K-band photometry of the Sculptor dSph galaxy, complementing this with optical V and I-band data from the ESO archive.

Figure 1 presents the Sculptor area observed, while table 1 summarises the observations.

### 2.1 The near-infrared data

Near-infrared observations in the  $J(1.25\mu\text{m})$  and  $K_s(2.15\mu\text{m})$  bands were made with the Cambridge Infrared Survey Instrument (Beckett et al. 1997, Mackay et al. 2000) on the du Pont 2.5m at Las Campanas Observatory. CIRSI

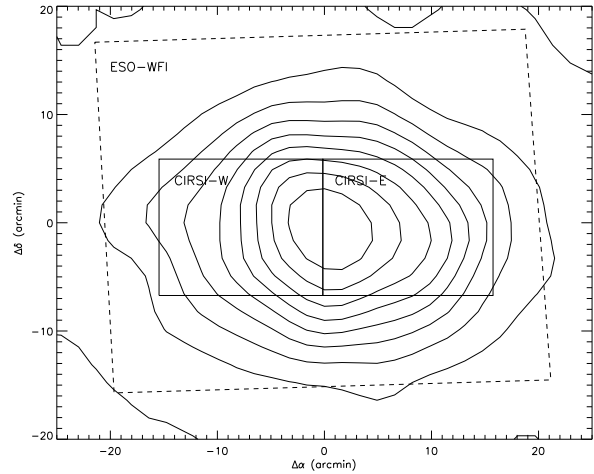


**Figure 1.** Field of view of the CIRSI and ESO-WFI data. The contours are from Irwin & Hatzidimitriou (1995). Sculptor's core and tidal radii are respectively 5.8 and 75 arcminutes.

is a mosaic imager consisting of four Rockwell 1k x 1k detectors. The pixel scale is  $0.2 \text{ arcsec pixel}^{-1}$ . The gaps between the detectors being comparable to the detector size, four dither sets are needed to fill the mosaic image, leading to a field of view of about  $13 \times 13 \text{ arcmin}^2$ . For each dither set, 9 dither frames are taken with offsets of about 10 arcsec. Each dither frame is observed in 5 loops of 20 seconds exposure time each. The total exposure time per mosaic is then 900s. Two mosaics were taken at the centre of the Sculptor dwarf spheroidal, as pictured in figure 1.

#### 2.1.1 CIRSI data reduction

The data reduction was made using an updated version of the InfraRed Data Reduction (IRDR) software package, first developed by Sabbey et al. (2001). A summary of the full process is given here. The updated version of IRDR with its documentation are available at <http://www.ast.cam.ac.uk/~optics/cirsi/software>. A fuller description is provided by Babusiaux & Gilmore (2005), in their presentation of a CIRSI study of the Galactic bulge and bar.

First each image is corrected for non-linearity. The dark current for the relevant exposure time is then subtracted. The data are flatfield corrected using lamp-on domeflats subtracted with lamp-off domeflats and normalized to the first detector sensitivity. These flatfields are also used to detect bad pixels and create weight maps, used during the dither frame coaddition.

The sky is subtracted in two passes. A first pass sky image is made by median combining the nearest loop-combined frames of the dither set. After a first dither frame coaddition, object masks are produced using SExtractor source extraction (Bertin & Arnouts 1996). A masked frame is created from this source-detection list, with an enlarged area around each detected source being used. This object-masked frame is used to make a second pass sky subtraction on each loop.

Spatial offsets between loop-combined dither frames are computed by cross-correlating object pixels mapped by SE-

**Table 1.** Log of the Sculptor observations. The exposure time format (d x n x exp) lists ‘n’, the number of short integrations on a specific centre (‘loops’), and ‘d’, the number of slightly offset (‘dither’) pointings. The seeing conditions, measured from the images, are indicated by the PSF FWHM (in arcsec) with the corresponding range during the mosaic observations with CIRSI.

Instrument	Field	Filter	Date	Exposure (secs)	seeing (″)
CIRSI	Sculptor-West	J	2001-09-04	9 x 5 x 20	1.02-1.4
		K <sub>s</sub>	2001-09-03	9 x 3 x 45	0.8-0.9
	Sculptor-East	J	2001-09-04	9 x 5 x 20	1.14-1.4
		K <sub>s</sub>	2001-09-03	9 x 5 x 20	0.96-1.3
ESO WFI	Sculptor	V	1999-07-22	3 x 300, dit-3	1.00
		I	1999-07-22	3 x 300	0.91

tractor. Dither frames are then coadded using a weighted bi-linear interpolation, excluding bad pixels.

Finally, the astrometry is calibrated by correlating the SExtractor’s object catalogue with the USNO-A2 catalogue.

### 2.1.2 CIRSI photometry

Once the data are reduced, we use the IRAF photometry routines. Source are detected using the IRAF DAOFIND procedure, with a significance threshold set at five-sigma. Aperture photometry is then obtained using the IRAF PHOT task. The aperture radius is assigned for each dither frame to the measured PSF FWHM. Observations of standard stars from Persson et al. (1998) were obtained each night, and were used to derive the magnitude zero-point of each night. Standard star photometry used an aperture photometry radius of 20 pixels, equivalent to a diameter of 8 arcsec. The internal zero point dispersion derived from multiple observations of the standard stars during a night is 0.013 mag in J and 0.008 mag in K. The instrumental magnitudes derived using the psf-fwhm aperture are corrected for aperture effects using the curve-of-growth method (Stetson 1990), implemented with the IRAF MKAPFILE task applied to selected bright isolated stars. Airmass corrections of  $k_J=0.1$  and  $k_K=0.08$  mag per air-mass (Persson et al. 1998) are applied to the photometry. Finally, images detected near the borders of the images are eliminated, so that only stars observed in all the dither frames are kept. False detections located in the wings of highly saturated stars are manually deleted.

The photometric calibration was checked by correlating the brightest stars with the 2MASS catalogue. The CIRSI K<sub>s</sub> photometry is consistent with the 2MASS photometric system. However, an offset in the J-band photometry of  $J_{(CIRSI)} - J_{(2MASS)} = -0.042 \pm 0.005$  is observed. This is due to the 2MASS J-band filter being more extended into the atmospheric water absorption features at around 1.1 and 1.4  $\mu\text{m}$  (Carpenter 2001) than is the filter used for CIRSI.

The 5- $\sigma$  magnitude completeness limits are about J $\sim$ 20 and K<sub>s</sub> $\sim$ 18.8. The photometric errors are about 0.025 mag for J $<$ 17, 0.08 mag at J=20, 0.022 mag for K<sub>s</sub>  $<$ 16, and 0.08 mag at K<sub>s</sub>=18.8.

## 2.2 The optical data

The optical data were obtained from the ESO 2.2m telescope Wide Field Imager archive. They consist of 3x300s dithered exposures in V and I. Each of the eight 4kx2k CCDs in the

ESO 2.2m WFI covers around 8 arcmin x 16 arcmin of sky at a sampling of 0.238 arcsec per pixel, comparable with the CIRSI data. The total field of view of the WFI is about 33 arcmin x 33 arcmin, including small gaps of around 10 arcsec between CCDs. This field of view entirely covers the observed CIRSI fields (figure 1).

The WFI data were processed using a variant of the standard optical pipeline described by Irwin & Lewis (2001). After trimming, bias-correcting, flatfielding and gain normalisation, the I-band exposures were additionally de-fringed using a I-band fringe frame derived from the 3 I-band science images. To generate the fringe frame, the 3 dithered I-band exposures were object masked, combined with rejection to remove residual artifacts, and then further filtered to improve the local signal-to-noise ratio.

Object catalogues were generated for each individual processed science frame and used to define, and refine, the World Coordinate System (WCS) for each frame, by comparison with the online APM plate catalogues. After updating the 2D images with the derived WCS, the 3 V and 3 I frames of Sculptor were stacked with cosmic ray rejection, using the WCS for coalignment, and confidence maps, derived from the flatfield frames and bad column lists for each CCD, to aid in rejection.

Final object catalogues were then derived from the stacked frames, and used both to update the WCS and to provide morphological classification information for each detected object. Object detection proceeds via a search for contiguous pixels at a threshold above the local sky; following detection a series of object parameters are derived. These latter are used to generate position, flux and shape information for use in later processing stages (Irwin 1985, Irwin 1997). The basic photometric measurement used is an aperture flux estimate with radius set to the average FWHM in the stacked frames. Additionally, all detected images have a series of fixed aperture measures produced (scaled to the basic aperture size used) in order to automatically derive aperture corrections for stellar images for each CCD.

Archive observations of Landolt (1992) standard fields define native system zero-points in each passband using the colour equations for WFI available on the ESO web site. The gain-correction in the previous stage ensures that all CCDs are on the same internal system, normalised to CCD1. However scattered light leads to a variation of the photometric zero points across the mosaic (Manfroid & Selman 2001). From the standard field observations, a correction term of  $1.5r^2$ , with r being the distance in degrees from the optical

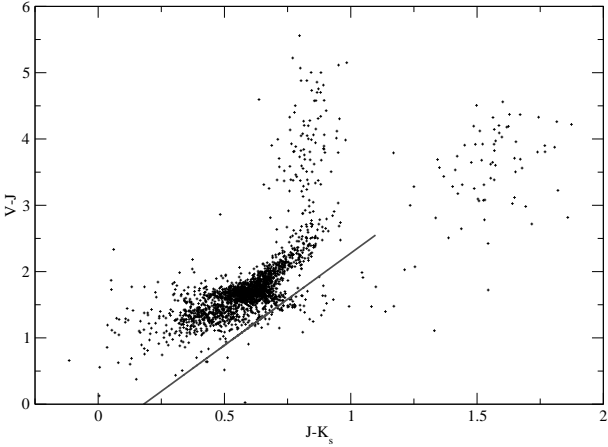


**Figure 2.** The V-J vs  $J-K_s$  colour-colour diagram of all point sources detected in V,I,J and  $K_s$ . The solid line shows the quasar selection criterion from the KX method (Warren et al. 2000).

axis, was found to be a good approximation of the effect of the scattered light. Overall, this provides a zero-point calibration with 1-2% accuracy.

The  $5\text{-}\sigma$  magnitude completeness limits are about  $V\sim 24$ ,  $I\sim 22.5$ , so that the censorship on the data is due only to the CIRSI J and  $K_s$  photometric limits. The errors are smaller than 0.01 mag in V and 0.02 in I for magnitudes brighter than  $V\sim 21.5$  and  $I\sim 19.5$ .

### 3 PHOTOMETRY OF THE SCULPTOR DSPH GALAXY

Our next task is to generate a list of point-sources which are stellar members of the Sculptor dSph galaxy. Extended objects are readily eliminated from further consideration using the morphological flags from the optical pipeline.

#### 3.1 Selection of Sculptor stars

The VJK colour-colour diagram, figure 2, allows the detection of three other point-source populations unrelated to the Sculptor dSph galaxy. Red quasars are clearly seen with colours which are too red to correspond to any star. All sources with  $J-K_s > 1$  were eliminated. A stream of stars with  $J-K_s$  about 0.8 mag and V-J colour redder than 3 mag can be seen. They are foreground low-mass dwarfs (e.g. Leggett 1992); these can be eliminated, without discarding any Sculptor stars, by excluding all stars redder than the colour of the tip of the Sculptor giant branch in all relevant colour-colour CMDs (e.g.  $V-I > 1.9$ ). A number of probable blue quasars can be seen bluer in V-J than the main stellar locus of Sculptor and foreground stars. These are selected and eliminated according to the KX method criterion (Warren et al. 2000), which is shown as the solid line in figure 2. Remaining foreground Galactic stars are minimised by our selection inside each colour-magnitude diagram of the location of Sculptor member stars, as described further below.

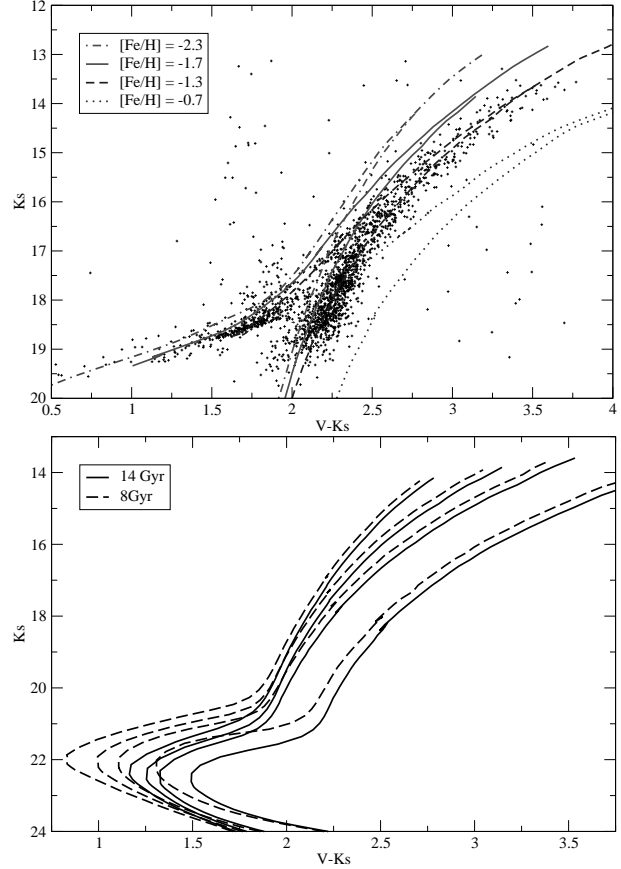


**Figure 3.** Theoretical isochrones of the Padova group (a) AGB and RGB isochrones for an age of 14 Gyr and for metallicities  $[\text{Fe}/\text{H}] = -2.3, -1.7, -1.3, -0.7$  dex from left to right. The data points are our photometry. (b) The RGB and main sequence turn-off for ages 14 and 8 Gyr and for the same four metallicities as in the top panel.

#### 3.2 The Sculptor Colour-Magnitude diagrams

It is apparent from figure 3a. that there is a significant real width to the RGB of Sculptor in the  $(V-K_s, K_s)$  colour-magnitude diagram, confirming several previous studies of Sculptor CMD. The RGB photometric width is about  $\Delta(V-K_s) = 0.3$  at magnitude  $K_s = 16$ , where the photometric measurement errors are 0.023 mag.

To determine the origin of this dispersion, theoretical isochrones from the Padova group, given in the ESO-WFI and 2MASS photometric systems by respectively Girardi et al. (2002) and Bonatto et al. (2004), have been overlaid on the Sculptor's CMDs, using a distance modulus  $(m-M)_0 = 19.54$  and an extinction  $E(B-V) = 0.02$  (Mateo 1998). The extinction is derived in the different photometric bands using the Cardelli et al. (1989) extinction curve.

Figure 3b shows theoretical RGB isochrones for metallicities  $Z = 0.0001, 0.0004, 0.001$  and  $0.004$  with solar mixture, and ages 8 and 14 Gyr. It can be seen that the RGB is much more sensitive to metallicity than to age. The main sequence turn-off, which is more sensitive to age, was used by Monkiewicz & et al. (1999) to derive an age of  $15 \pm 2$  Gyr for Sculptor. The results of Dolphin (2002) and Rizzi et al. (2004) confirm the predominance of old stars in Sculptor. We therefore adopted isochrones of age 14 Gyr for figure 3a.

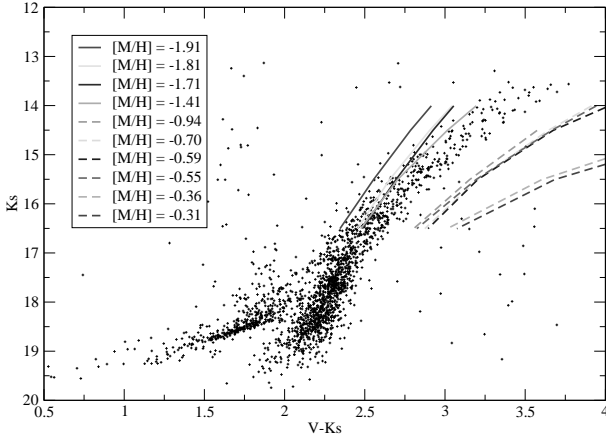


**Figure 4.** Sculptor photometric data from this study (points), together with the fiducial RGB lines for the sample of Galactic globular clusters from Ferraro et al. (2000), with their global metallicities as defined by Ferraro et al. (1999) indicated.

These isochrones clearly confirm the presence of a metallicity spread within the Sculptor RGB stars.

The colour magnitude diagrams can also be compared directly to globular cluster observations. Ferraro et al. (2000) and Saviane et al. (2000) provide fiducial lines for the RGB of Galactic globular clusters for a wide range of metallicity, in the (V,J,K) and (V,I) photometric systems. Figure 4 shows the fiducials of Ferraro et al. (2000) globular clusters on the (V-K<sub>s</sub>,K<sub>s</sub>) colour-magnitude diagram of Sculptor. The transformation from absolute to relative magnitudes is the same as the one applied for the theoretical isochrones. However the V and K magnitudes are not on the same photometric system as ours, leading to expected photometric differences of the order of 0.1 mag. Considering that globular clusters tend to have alpha-enhanced element ratios, whereas the Sculptor stars do not, we indicate their global metallicities as defined by Ferraro et al. (1999). The definition of this global metallicity scale and how it can be translated into [Fe/H] for Sculptor is discussed in section 4. Here again a metallicity spread is confirmed as being consistent with the width of the Sculptor RGB. Figure 4 illustrates that all stars in Sculptor are more metal-poor than [M/H] = -1.0.

The spread of the RGB in the (J-K<sub>s</sub>,K<sub>s</sub>) and (V-I,I) CMDs is smaller and more sensitive to photometric errors than in (V-K<sub>s</sub>,K<sub>s</sub>). According to Saviane et al. (2000), a variation of metallicity from -2.0 to -1.5 dex results in a difference in V-I of 0.04 mag at I = -2 (one magnitude brighter than the RGB bump), while according to Ferraro et al. (2000), the same variation of metallicity at K = -3 results in a variation of 0.2 mag in V-K. Considering the relative photometric errors in V, I and K<sub>s</sub>, this means that V-K<sub>s</sub> is 1.7 times as sensitive to metallicity as is V-I. We will therefore use preferentially the (V-K<sub>s</sub>,K<sub>s</sub>) CMD in the following to derive photometric metallicity indicators.

#### 4 THE RGB AND AGB BUMPS

Local maxima are observed in the luminosity function of the giant branch of old metal-poor stellar populations. These

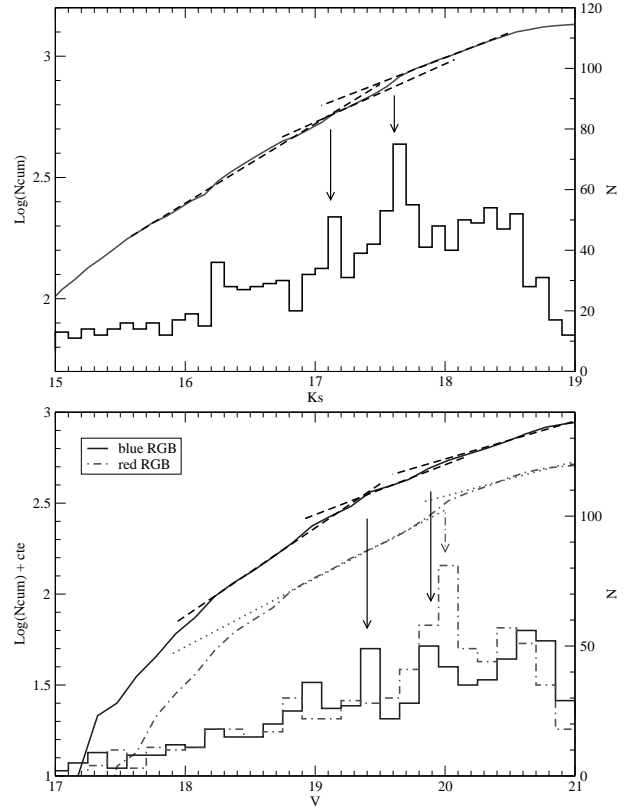


**Figure 5.** Luminosity Function (LF) and cumulative LF (a) in the K<sub>s</sub> band for all stars, (b) in the V band separately for stars redder and bluer than the giant branch mean fiducial.

RGB and AGB bumps are well known features of the colour-magnitude diagrams of globular clusters (e.g. Ferraro et al. 1999). Those two bumps are detected in all our visible and near-infrared bands (table 2), as illustrated in figure 5 for the V and K<sub>s</sub> bands. To allow us to compare the absolute magnitudes of these features in Sculptor with other studies, the ESO WFI V and I photometry was converted into the standard Johnson photometry using the Girardi et al. (2002) isochrones in those two filter systems. At the location of the bumps,  $(V - I)_J = 0.96$ , a given simulated star of the isochrones present the colours  $V_J - V_{WFI} = -0.06$  and  $I_J - I_{WFI} = 0.1$ . As previously, the conversion to absolute magnitudes assumes a distance modulus of 19.54 mag and  $E(B-V) = 0.02$ . Errors in the determination of the bump location are of about 0.1 mag.

Majewski et al. (1999) also detected those two bumps within the central 10', but associated the second one with the RGB bump of a more metal-poor population. Indeed, the AGB bump of a population of metallicity  $[Fe/H] \simeq -1.5$  is located at the same position on the CMD as is the RGB bump of a population of metallicity  $[Fe/H] \simeq -2$ . The V magnitude of the second bump is consistent with the value of  $M_V(AGB\text{bump}) = -0.3 \pm 0.1$  used by Ferraro et al. (1999). Its clear detection can be explained by the fact that the luminosity level of the AGB bump stays fairly constant with the cluster metallicity (e.g. Castellani et al. 1991). The AGB bump being always bluer than the RGB, it explains the detection of this second bump on the blue side of the RGB by Majewski et al. (1999). Using, as they did, a division of

**Table 2.** Magnitudes of the RGB and AGB bumps. See the text for a definition of the photometric system.

	$m_{V_{WFI}}$	$m_{I_{WFI}}$	$m_J$	$m_{K_s}$	$M_{V_J}$	$M_{I_J}$	$M_J$	$M_{K_s}$
RGB bump	19.92	18.83	18.23	17.61	0.26	-0.64	-1.33	-1.94
AGB bump	19.40	18.38	17.75	17.13	-0.26	-1.09	-1.81	-2.42

the giant branch into a red and blue part (figure 6), we not only find as expected the second bump on the blue side of the giant branch, but also the RGB bump shifted by about 0.2 magnitudes (figure 5b), which is consistent with a variation in metallicity. If the second bump is to be due to a distinct metal-poor population, being clearly detected at all wavelengths, this second population should also show a clear imprint on the tip of the red giant branch. No such distinct second RGB can be detected (figures 3a. and 4). We then conclude that the second bump is the AGB bump.

The V magnitudes of the HB and the RGB bump are good indicators of the metallicity (e.g. Ferraro et al. 1999). The peculiar shape of Sculptor’s HB however makes the determination of its mean V magnitude unreliable (figure 7). The V magnitude of the RGB bump leads to a global metallicity of  $[M/H] = -1.30 \pm 0.12$  from the calibration of Ferraro et al. (1999). Its  $K_s$  magnitude leads to  $[M/H] = -1.39 \pm 0.14$  according to Cho & Lee (2002), while it leads to  $[M/H] = -1.19 \pm 0.12$  from the new calibration of Valenti et al. (2004). Those calibrations were made using the relation of Salaris et al. (1993):

$$[M/H] = [Fe/H] + \log(0.638 * 10^{[\alpha/Fe]} + 0.362) \quad (1)$$

Sculptor does not seem to present a strong enhancement of alpha-elements: Shetrone et al. (2003) measured for 5 stars the following values for  $[\alpha/Fe]$ : 0.18, 0.13, 0.13, -0.01 and 0.23 (table 2 of Tolstoy et al. 2003). For  $[\alpha/Fe]=0.13$ ,  $[M/H]=-1.3$  can be translated to  $[Fe/H]=-1.4$  by equation 1.

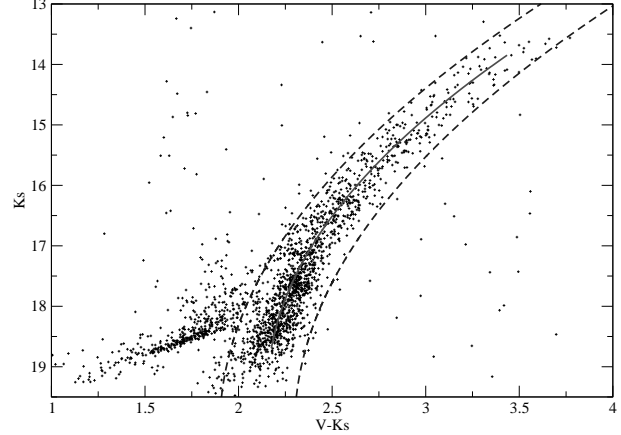
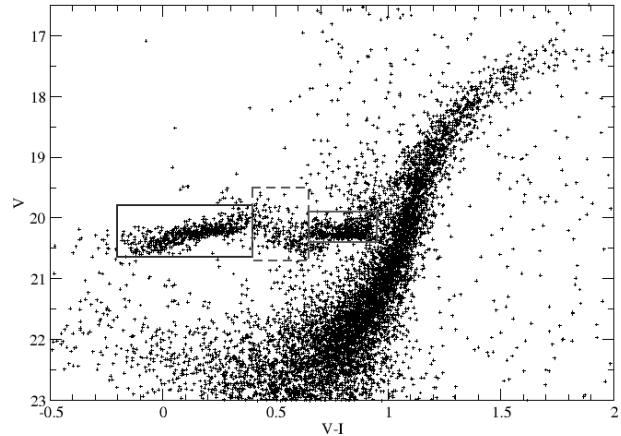
It should be stressed that the indicated errors do not take into account the uncertainty in the distance modulus, estimated to be 0.08 mag in Mateo (1998). Another metallicity indicator, independent of the distance modulus and of zero point calibration errors, is the difference between the AGB and RGB bump luminosities. From Ferraro et al. (1999), with  $\delta V_{AGBbump}^{RGBbump} = 0.52 \pm 0.14$ , we can derive  $[M/H] = -1.4 \pm 0.2$ .

Those metallicity indicators agree with the previous comparisons of the RGB morphology with theoretical isochrones and globular clusters (figure 3a and figure 4).

## 5 THE METALLICITY DISTRIBUTION FUNCTION

The mean fiducial of the Sculptor red giant branch was computed through a least squares fit to a second order polynomial on the  $(V-K_s, K_s)$  CMD. Horizontal branch stars and foreground stars have been eliminated by selecting only the stars 0.2 magnitudes away from the mean fiducial (figure 6). Only the giant branch stars brighter than  $K_s=18.7$  and up to the RGB tip ( $K_s > 13.8$ ) have been selected. As the AGB stars occupy the same location on the CMD as the most metal poor RGB population, no attempt to discard AGB stars was made.

We derive the metallicity distribution of those selected

**Figure 6.** Least square fit of a second order polynomial to the Sculptor giant branch. The dashed curves frames the stars selected for the giant branch studies.**Figure 7.** Sculptor  $(V-I, V)$  CMD. The boxes indicate how the HB index was computed, selecting the B, V and R stars.

Sculptor giant branch stars using the Padova isochrones described previously. Each isochrone of figure 3a can be approximated by a second order polynomial:

$$V - K_s = a_0 + a_1 K_s + a_2 K_s^2 \quad (2)$$

A second order polynomial regression of those coefficients as a function of the metallicity of the isochrones is obtained:

$$a_i = a_{(i,0)} + a_{(i,1)}[Fe/H] + a_{(i,2)}[Fe/H]^2 \quad (3)$$

By inverting equation 2, each point in the  $(V-K_s, K_s)$  CMD can then be assigned an estimate of its metallicity. Taking into account only the uncertainty of the accuracy on the polynomial regression of equations 2 and 3 and the photometric errors, the typical uncertainty in the resulting measurement of the metallicity of a individual star is smaller than 0.04 dex.

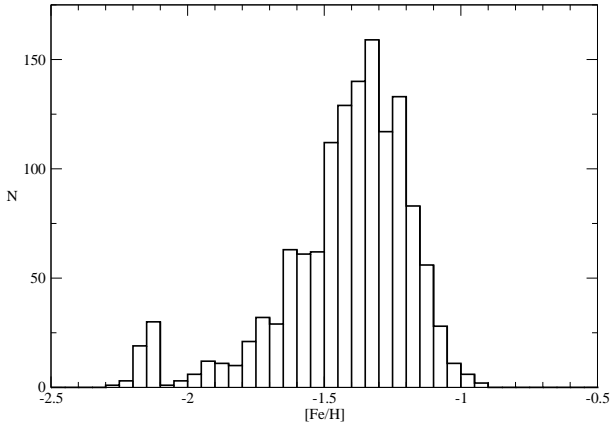


**Figure 8.** Photometric metallicity distribution function as derived using theoretical isochrones.

The resulting metallicity distribution function is represented in figure 8. The secondary peak at  $[\text{Fe}/\text{H}] = -2.2$  is an artefact due to AGB stars and should be ignored. The mean metallicity obtained is  $[\text{Fe}/\text{H}] = -1.42$  with a dispersion of 0.2 dex. This mean metallicity is in agreement with the value obtained from the RGB bump. A comparison of those metallicity estimates with the literature is given in the discussion section.

## 6 METALLICITY GRADIENT INDICATORS

### 6.1 The Giant Branch

Since the RGB in our photometric system provides a good indicator of metallicity, we studied its variation with radius as a test of a possible metallicity gradient in Sculptor.

The metallicity indicators derived in the previous section have been studied as a function of radius. The central 10 arcminutes of Sculptor has zero ellipticity (Irwin & Hatzidimitriou 1995), so as our data do not extend beyond a radius of 15 arcminutes, we use a simple circular annulus. Figure 9 show that no metallicity gradient is detected within our data. This gives an upper limit of 0.03 dex for the metallicity gradient within twice the core radius of Sculptor.

### 6.2 The Horizontal Branch

The horizontal branch of Sculptor can be clearly divided into a blue (B) and a red (R) part, lying on either side of the instability strip (V). The ratio of the number counts of those different parts, quantified by the HB index  $(\text{B}-\text{R})/(\text{B}+\text{V}+\text{R})$ , is dependent on the metallicity. But there is a well known ‘second parameter problem’, which could be age (e.g. Lee et al. 1994).

The HB index was computed from the (V-I,V) CMD, as illustrated in figure 7, for the same radial annuli as used for the RGB study. Both the full ESO WFI field of view data and the sub-area in common with the CIRSI field of view are presented in figure 10. A K-S test for the hypothesis that the red and blue horizontal branch stars have the same radial distribution gives a significance level of  $10^{-9}\%$ . This

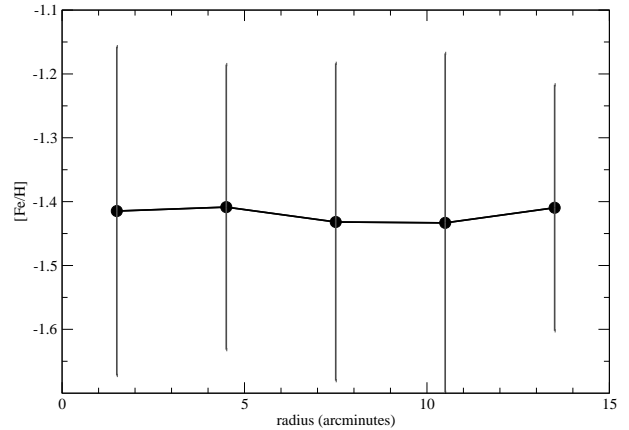


**Figure 9.** Mean metallicity, as estimated in section 5, as a function of radius. The vertical line show the measured dispersion around this value.

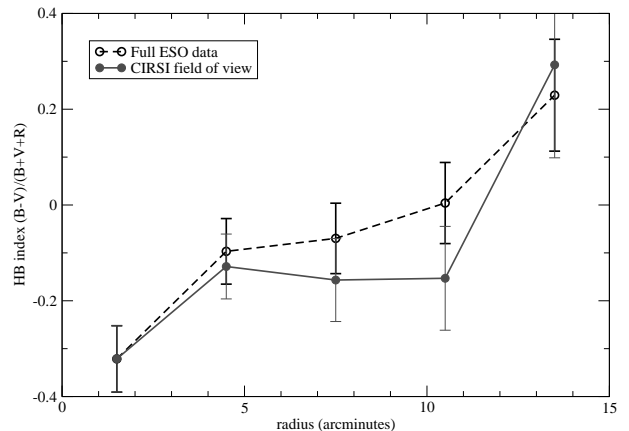


**Figure 10.** The HB index against radius for all the ESO-WFI data and stars only within the CIRSI field of view (figure 1).

confirms the HB gradient detected by Hurley-Keller et al. (1999) and Majewski et al. (1999).

The Lee et al. (1994) models give theoretical isochrones that show, for an HB index between -0.5 and 0.5 and a given age, a linear relation between the HB index and the metallicity:

$$[\text{Fe}/\text{H}] \simeq -0.34 * \text{HBindex} + cte \quad (4)$$

The observed gradient in HBindex of about 0.5 then corresponds to a gradient in metallicity of 0.17 dex. Considering the upper limit of 0.04 dex for a metallicity gradient derived previously from the RGB morphology, an age gradient is required to explain the observed HB gradient. As always when discussing HB morphology however, one must recall that the ‘second parameter problem’ is not yet solved and that another parameter may influence the HB morphology.

The simplest conclusion is that a small gradient in mean age is apparent in Sculptor and that an eventual small metallicity gradient associated with it would have a too small effect on the RGB compared to the large abundance dispersion to be detected.

## 7 CONCLUSIONS AND DISCUSSION

The combination of near-infrared photometry from CIRS with optical data from the ESO WFI, allowed a detailed study of the Sculptor dwarf spheroidal giant branch morphology. We confirm that the broad giant branch of Sculptor demonstrates an intrinsic metallicity spread (e.g. Da Costa 1984, Schweitzer et al. 1995, Kaluzny et al. 1995, Majewski et al. 1999). From our photometric study we quantify this spread into a metallicity range of  $\Delta[Fe/H] = 0.75$  dex. The RGB and AGB bumps are detected in all the optical and near-infrared luminosity functions, excluding the substantial metal-poor contribution to Sculptor's metallicity distribution proposed by Majewski et al. (1999). We derive a mean metallicity within two core radii in Sculptor of about  $[Fe/H] = -1.4$  from both the RGB and AGB bumps magnitudes and isochrones fitting. Our mean metallicity and the metallicity range are higher than those derived in Da Costa (1984) from photometry of the RGB and in Kaluzny et al. (1995) from RR Lyrae stars: these results were summarized in the Mateo (1998) review as a mean of  $[Fe/H] = -1.8 \pm 0.1$  with a spread of 0.3 dex. However our photometry is in agreement with the metallicity estimations from Sculptor RR Lyrae stars of Kovács (2001) and CaII triplet observations of 37 stars of Tolstoy et al. (2001). It is in excellent agreement with the very recent spectroscopic survey of Tolstoy et al. (2004), whose derived metallicity distribution inside two core radii indicates a mean metallicity of  $-1.4$  dex, and metallicity range of about 1 dex. Their data show the population structure is complex, with the more metal-poor part of the distribution function becoming dominant at radii beyond those we have studied here.

We do not detect a gradient in the RGB morphology within a radius of  $13'$ , 2.2 times the Sculptor core radius. Although Harbeck et al. (2001) and Tolstoy et al. (2004) find a metallicity gradient in Sculptor, our result is in agreement with their data. Indeed figure 6 of Harbeck et al. (2001) shows that the radial distribution of blue and red RGB stars begins to differ only after  $13'$ . Figure 3 of Tolstoy et al. (2004), based on spectroscopic data, indicates that a metallicity gradient is indeed visible only beyond this radius. On the other hand, we do detect at high significance a gradient in the horizontal branch (HB) morphology, confirming the results of Hurley-Keller et al. (1999) and Majewski et al. (1999). As this cannot be explained by metallicity, the most likely second parameter could be age. Hurley-Keller et al. (1999) did not find evidence for a gradient in the main-sequence turn off, leading to an upper limit of a 2 Gyr variation at constant metallicity. According to the models of Lee et al. (1994) a small variation in age of even a few Gyr leads to a strong variation in the HB morphology. Age could then still be the second parameter. Moreover,  $[Fe/H]$  and age are not the only variables which can affect the HB morphology, but also other element abundances, in particular the  $[O/Fe]$  ratio (Lee et al. 1994). Hurley-Keller et al. (1999) detected another population presenting a gradient in Sculptor: a 'spur' of stars extending  $\sim 0.7$  mag above the old main sequence turn off. They conclude that it cannot be explained by the presence of an intermediate age population, preferring the interpretation of the spur as a binary sequence, and speculate that it could be related to the variation of the HB morphology.

No significant intermediate age population has been found in Sculptor, excluding star formation within the last 5 Gyr. The large metallicity spread requires extended star formation, while the evidence of low alpha-element enhancement implies extended star formation and self-enrichment over a period of at least 1 Gyr: quite long enough to affect the HB morphology. The HB morphology gradient implies that the most recent star formation episode occurred in the centre of the galaxy, consistent with naive expectation that gas is more easily retained deeper in the galaxy potential well. Indeed in most dwarf galaxies observed with sufficiently deep wide-field imaging, populations gradients have been found with the younger stars being more centrally concentrated (e.g. Saviane et al. 2001 and references therein). Our lack of detection of a metallicity gradient may be explained by the age-metallicity degeneracy that would hide a small age and metallicity difference and by the stronger dependence of the HB on other parameters such as the oxygen abundance, stellar rotation or binarism, as already suggested by Hurley-Keller et al. (1999) and Majewski et al. (1999).

All this could be consistent for Sculptor with a single period of star formation extended in time for of the order of a few Gyr. Tolstoy et al. (2003) conclude that their study of the element abundances are consistent with a closed-box chemical evolution scenario. The small dynamical mass of dwarf spheroidals such as Sculptor means that their binding energy is small compared to the energy released by several supernovae, which leads the high metallicity spread and relatively high mean metallicity derived for Sculptor puzzling: how did the gas stay bound long enough to have an extended star formation and gas enrichment? The star formation rate should be low to allow the chemical enrichment to proceed gradually. Hydrodynamical simulations are trying to answer this question (e.g. Carraro et al. 2001, Carigi et al. 2002).

## ACKNOWLEDGMENTS

We are grateful to Jacco van Loon for his assistance with the CIRS observations. We thank the anonymous referee for helpful comments. The development and construction of CIRS was made possible by a grant from the Raymond and Beverly Sackler Foundation.

## REFERENCES

- Babusiaux C., Gilmore G., 2005, MNRAS, in press
- Beckett M. G., Mackay C. D., McMahan R. G., Parry I. R., Piche F., Ellis R. S., 1997, in Proc. SPIE Vol. 2871, p. 1152-1159, Optical Telescopes of Today and Tomorrow, Arne L. Ardeberg; Ed. CIRS: the Cambridge Infrared Survey Instrument. pp 1152-1159
- Bertin E., Arnouts S., 1996, A&A Suppl. Ser., 117, 393+
- Bonatto C., Bica E., Girardi L., 2004, A&A, 415, 571
- Bouchard A., Carignan C., Mashchenko S., 2003, AJ, 126, 1295
- Cardelli J. A., Clayton G. C., Mathis J. S., 1989, ApJ, 345, 245
- Carigi L., Hernandez X., Gilmore G., 2002, MNRAS, 334, 117



- Carignan C., Beaulieu S., Côté S., Demers S., Mateo M., 1998, *AJ*, 116, 1690
- Carpenter J., 2001, *AJ*, 121, 2851+
- Carraro G., Chiosi C., Girardi L., Lia C., 2001, *MNRAS*, 327, 69
- Castellani V., Chieffi A., Pulone L., 1991, *ApJS*, 76, 911
- Cho D., Lee S., 2002, *AJ*, 124, 977
- Da Costa G. S., 1984, *ApJ*, 285, 483
- Dolphin A. E., 2002, *MNRAS*, 332, 91
- Ferraro F. R., Messineo M., Fusi Pecci F., de Palo M. A., Straniero O., Chieffi A., Limongi M., 1999, *AJ*, 118, 1738
- Ferraro F. R., Montegriffo P., Origlia L., Fusi Pecci F., 2000, *AJ*, 119, 1282
- Girardi L., Bertelli G., Bressan A., Chiosi C., Groenewegen M. A. T., Marigo P., Salasnich B., Weiss A., 2002, *A&A*, 391, 195
- Harbeck D., Grebel E. K., Holtzman J., Guhathakurta P., Brandner W., Geisler D., Sarajedini A., Dolphin A., Hurley-Keller D., Mateo M., 2001, *AJ*, 122, 3092
- Hurley-Keller D., Mateo M., Grebel E. K., 1999, *ApJ*, 523, L25
- Irwin M., 1985, *MNRAS*, 214, 575
- Irwin M., 1997, *Instrumentation for Large Telescopes*. Cambridge University Press
- Irwin M., Hatzidimitriou D., 1995, *MNRAS*, 277, 1354
- Irwin M., Lewis J., 2001, *New Astronomy Review*, 45, 105
- Kaluzny J., Kubiak M., Szymanski M., Udalski A., Krzeminski W., Mateo M., 1995, *A&AS*, 112, 407
- Kovács G., 2001, *A&A*, 375, 469
- Landolt A. U., 1992, *AJ*, 104, 340
- Lee Y., Demarque P., Zinn R., 1994, *ApJ*, 423, 248
- Leggett S. K., 1992, *ApJS*, 82, 351
- Lynden-Bell D., 1976, *MNRAS*, 174, 695
- Mackay C. D., McMahon R. G., Beckett M. G., Gray M., Ellis R. S., Firth A. E., Hoenic M., Lewis J. R., Medlen S. R., Parry I. R., Pritchard J. . M., Sabbey C. S., 2000, in *Proc. SPIE Vol. 4008*, p. 1317-1324, *Optical and IR Telescope Instrumentation and Detectors*, Masanori Iye; Alan F. Moorwood; Eds. CIRSI: the Cambridge infrared survey instrument for wide-field astronomy. pp 1317–1324
- Majewski S. R., Siegel M. H., Patterson R. J., Rood R. T., 1999, *ApJ*, 520, L33
- Manfroid J., Selman F., 2001, *The Messenger*, 104, 16
- Mateo M. L., 1998, *ARA&A*, 36, 435
- Monkiewicz J., et al. 1999, *PASP*, 111, 1392
- Persson S. E., Murphy D. C., Krzeminski W., Roth M., Rieke M. J., 1998, *AJ*, 116, 2475
- Rizzi L., Held E. V., Bertelli G., Saviane I., 2004, *Memorie della Societa Astronomica Italiana*, 75, 110
- Sabbey C. N., McMahon R. G., Lewis J. R., Irwin M. J., 2001, in *ASP Conf. Ser. 238: Astronomical Data Analysis Software and Systems X Infrared Imaging Data Reduction Software and Techniques*. pp 317–+
- Salaris M., Chieffi A., Straniero O., 1993, *ApJ*, 414, 580
- Saviane I., Rosenberg A., Piotto G., Aparicio A., 2000, *A&A*, 355, 966
- Saviane I., Held E. V., Momany Y., Rizzi L., 2001, *Memorie della Societa Astronomica Italiana*, 72, 773
- Schweitzer A. E., Cudworth K. M., Majewski S. R., Suntzeff N. B., 1995, *AJ*, 110, 2747
- Shetrone M., Venn K. A., Tolstoy E., Primas F., Hill V., Kaufer A., 2003, *AJ*, 125, 684
- Stetson P. B., 1990, *PASP*, 102, 932+
- Tolstoy E., Irwin M. J., Helmi A., Battaglia G., Jablonka P., Hill V., Venn K. A., Shetrone M. D., Letarte B., Cole A. A., Primas F., Francois P., Arimoto N., Sadakane K., Kaufer A., Szeifert T., Abel T., 2004, *ApJ*, 617, L119
- Tolstoy E., Irwin M. J., Cole A. A., Pasquini L., Gilmozzi R., Gallagher J. S., 2001, *MNRAS*, 327, 918
- Tolstoy E., Venn K. A., Shetrone M., Primas F., Hill V., Kaufer A., Szeifert T., 2003, *AJ*, 125, 707
- Valenti E., Ferraro F. R., Origlia L., 2004, *MNRAS*, 354, 815
- Warren S. J., Hewett P. C., Foltz C. B., 2000, *MNRAS*, 312, 827